Chemical Engineering Journal 509 (2025) 161487

Contents lists available at ScienceDirect

Chemical Engineering Journal

journal homepage: www.elsevier.com/locate/cej

Functionalized dendritic memristor of Pt/MoS_2@LCO-PVA/Si for Mimicking synaptic behavior

Xueli Geng [a], Qin Gao [b,*], Jiangshun Huang [a], Juan Gao [a], Pengzhan Li [a], Yihang Liu [a], Qiaofeng Yang [a], Xinghe Li [a], Hao Zhang [c], Zhisong Xiao [a,b], Mei Wang [a], Paul K. Chu [d], Anping Huang [a,*]

[a] School of Physics, Beihang University, Beijing 100191, PR China
[b] School of Applied Science, Beijing Information Science & Technology University, Beijing 102206, PR China
[c] School of Space and Earth Sciences, Beihang University, Beijing 100191, PR China
[d] Department of Physics, Department of Materials Science and Engineering, and Department of Biomedical Engineering, City University of Hong Kong, Tat Chee Avenue, Kowloon, Hong Kong, PR China

ARTICLE INFO

Keywords:
Memristors
MoS_2 nanosheets
Dendrites
Synaptic Plasticity
Neurocomputing

ABSTRACT

Artificial synaptic memristors, with their adjustable and non-volatile resistance, present a promising path for neuromorphic computing (NC). Inspired by the salting-out producing dense fractal dendritic morphologies, a dendritic ion framework composed of $LiClO_4{\cdot}3H_2O$ (LCO) and polyvinyl alcohol (PVA) is prepared by spin coating. The functionalized dendritic Pt/MoS_2@LCO-PVA/Si memristor boasts 1,670 endurance cycles and a retention time exceeding 10^4 s. MoS_2 nanosheets act as the intermediate to improve ion transportation and storage, and the multi-local enhanced electric field is verified by multi-physics COMSOL simulation. Synaptic plasticity, such as spike-voltage-dependent plasticity, long-term potentiation/depression, and spike-timing-dependent plasticity are also investigated. The dendritic device achieves a digit recognition accuracy of 91.4 % according to simulations of artificial neural networks. The results reveal a new approach that expands the applications of NC.

1. Introduction

Spurred by the rapid advancement of artificial intelligence and the Internet of Things, neuromorphic computing (NC) architectures based on synapse components have attracted significant attention due to their in-memory computing capabilities and low power consumption [1–3]. Among them, the two-terminal memristor, featuring a simple metal-insulator-metal structure, non-volatility, and the ability to emulate biological synaptic behavior by modulating conductance states as synaptic weights, is especially promising [4,5]. The conductance state of memristor is primarily regulated by the formation and rupture of conductive channels under an applied electric field and driven by the migration of metal ions or vacancies [6,7,8]. However, these devices always suffer from severe temporal variations due to the random growth of conductive channels during switching, consequently posing a challenge for practical NC applications [9–11].

Several strategies have been proposed to regulate ion migration, for instance, incorporation of low-dimensional materials [12–14], elemental doping [15,16], and interface engineering [17,18]. Biomimetic methods, which emulate the structure and function of natural materials, have garnered significant attention for their potential to enhance device performance [19–21]. In particular, conductive channels inspired by natural phenomena can be used to optimize ion transport and storage. In biological systems, aligned ion channel proteins facilitate the selective passage of specific ions to serve as a confined pathway to regulate the ion concentrations and ensure reliable ion migration [22–24]. Similarly, intricate natural geometries with high transmissibility and directivity, such as hierarchical porous structures, multi-layered architectures, and fractal geometry, play a crucial role in controlling ions transport [25–28]. These efficient natural structures can serve as the blueprint for the design of constrained transport pathways to mitigate the inherent instability of ion movement.

* Corresponding authors at: School of Physics, Beihang University, Beijing 100191, PR China (A. Huang) and School of Applied Science, Beijing Information Science & Technology University, Beijing 102206, PR China (Q. Gao).
E-mail addresses: gaoqin@bistu.edu.cn (Q. Gao), aphuang@buaa.edu.cn (A. Huang).

https://doi.org/10.1016/j.cej.2025.161487
Received 29 November 2024; Received in revised form 8 February 2025; Accepted 10 March 2025
Available online 11 March 2025

Herein, a dendritic ionic framework (LCO-PVA), inspired by the growth of natural salt dendrites, is prepared and functionalized with MoS_2 nanosheets. The functionalized dendritic memristor (MoS_2@LCO-PVA) shows robust durability for 1,670 cycles, retention time of 10^4 s, and average SET voltage of 0.97 V. The MoS_2 nanosheets effectively limit the migration of Li^+ ions in the dendritic structure by generating a localized enhanced electric field under an applied voltage. The typical synaptic characteristics are simulated, and the digit recognition capability evaluated using an artificial neural network (ANN) shows an accuracy of 91.4 %. Our results demonstrate the significant potential of this memristor for artificial synapse simulation in image recognition applications.

2. Results and Discussion

Salt dendrites in nature display a random growth pattern characterized by both independent and interconnected fractal structures, as illustrated in Fig. 1(a). Fig. 1(b) shows the preparation progress of the PVA-LCO dendritic framework and Fig. S1 depicts the optical images of samples with different LCO doping concentrations (0 wt%, 10 wt%, 35 wt%, and 50 wt%). The temporal evolution of the dendritic structure is monitored by optical microscopy for a doping concentration of 35 wt%, as shown in Fig. 1(c). The *I-V* curves of the Pt/PVA-LCO/Si devices with different LCO doping concentrations are shown in Fig. S2, in which the memristive behavior is not observed.

MoS_2 nanosheets can store Li^+ due to multiple ion trapping sites, small volume expansion, and reversible conversion between the 2H (semiconductor) and 1 T (metal) phases [29,30]. Fig. 2(a) shows the schematic representation of the functionalized dendritic ion framework modified by MoS_2 nanosheets. The MoS_2 nanosheets are incorporated into the PVA-LCO solution, as shown in Fig. 2(a-I), and then stirred to ensure uniform dispersion by taking advantage of the good dispersion properties of PVA with MoS_2 nanosheets [31,32], resulting in the formation of a MoS_2@LCO-PVA solution shown in Fig. 2(a-II). The MoS_2@LCO-PVA structure with LCO doping concentrations of 0 wt%, 10 wt%, 35 wt%, and 50 wt% are prepared, and the scanning electron microscopy (SEM) images are displayed in Figs. S3 and 2 (a-III). The samples with LCO concentrations of 0 wt% and 10 wt% have no dendritic structures, as shown in Fig. S3(a) and Fig. S3(b), whereas the sample with an LCO concentration of 50 wt% shows a thin film composed of dense microrods, as shown in Fig. S3(c). It is noted that an independent and interconnected dendritic structure can be obtained when the doping concentration is 35 wt%, as shown in Fig. 2(a-III). The dendritic LCO-PVA structures act as a lithium source and provide a fast migration channel for Li^+ ions. The atomic force microscope (AFM) characterization of the thin film with different doping concentrations is presented in Figs. S4(a)-(d). When the LCO concentration is 35 wt% and 50 wt%, dominant dendritic structures and dense microrods appear, leading to a significant increase in surface roughness as shown in Figs. S4(c)-(d), respectively. In contrast, when the LCO concentration is 0 wt% and 10 wt%, the surface roughness is relatively low, likely due to the more uniform and smoother film morphology with fewer structural variations, as shown in Figs. S4(a)-(b), respectively. Energy-dispersive X-ray spectroscopy (EDS) confirms the random distribution of MoS_2 nanosheets in the MoS_2@LCO_{35}-PVA dendritic structure with 35 wt% LCO, as shown in Fig. 2(b). The Raman scattering spectrum of MoS_2 nanosheets in the dendritic structure in Fig. 2(c) features peaks corresponding to the E^1_{2g} and A_{1g} phonon modes of MoS_2 at 384.5 and 409.7 cm^{-1}, respectively. The difference between the two modes is 25.2 cm^{-1}, indicating that MoS_2 nanosheets are composed of multiple layers and confirming the presence of a 2H phase in MoS_2 [33].

Memristors with different LCO concentrations (0 wt%, 10 wt%, 35 wt

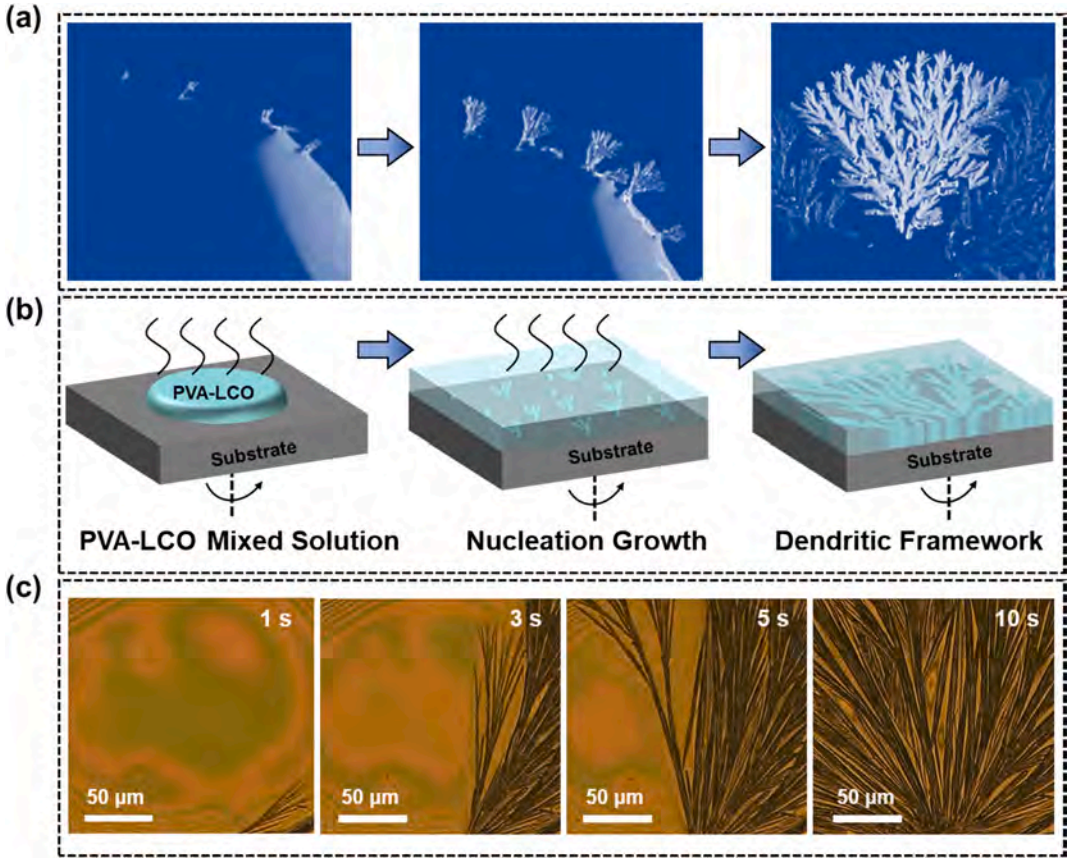

Fig. 1. (a) Growth progress of fractal salt dendrite structures in nature; (b) Schematic illustration of the dendritic ion framework preparation by spin coating; (c) Growth of the dendritic ion framework monitored by optical microscopy for an LCO doping concentration of 35 wt%.

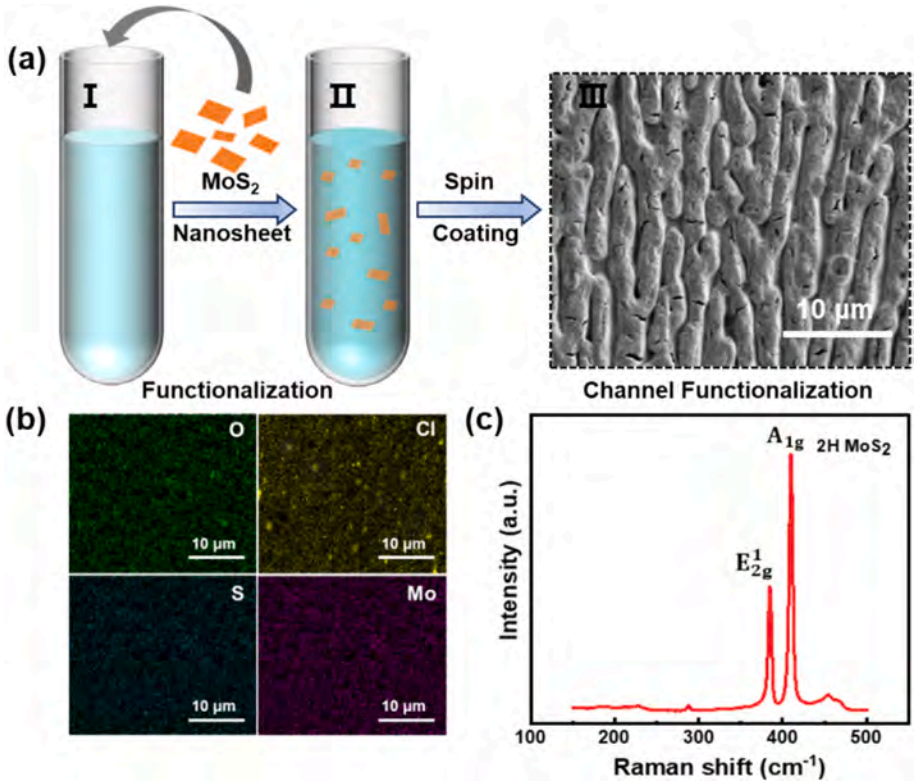

Fig. 2. (a) Schematic diagram of the PVA-LCO dendritic framework functionalized with MoS_2 nanosheets; (b) Elemental maps of O, Cl, Mo, and S shown in Fig. 1(a-III); (c) Raman scattering spectrum of the MoS_2 nanosheets in the dendritic framework.

%, and 50 wt%) are constructed, and their memristive characteristics are assessed, as shown in Fig. 3 and Fig. S5. Fig. 3(a) shows the schematic diagram of the Pt/MoS_2@LCO-PVA/Si device, and the corresponding cross-sectional SEM image for the sample with an LCO concentration of 35 wt% is depicted in Fig. 3(b), which reveals a clearly defined independent microrod structure. The thickness of the dendritic MoS_2@LCO-PVA layer is approximately 1.5 μm and the Pt layer is approximately 100 nm. The semi-logarithmic current–voltage (*I-V*) curves of the Pt/MoS_2@LCO_{35}-PVA/Si dendritic memristor with 35 wt% LCO show good performance with analog memristive properties, as shown in Fig. 3(c). 1,670 consecutive cycles are tested between –3 V and 2 V using the direct current (DC) sweeping mode, a voltage step of ± 0.01 V, and a compliance current (I_{cc}) of 0.01 A during the SET process. Fig. 3(d) shows that the high-resistance state (HRS) and the low-resistance state (LRS) are obtained for 1,670 cycles at the 0.1 V reading voltage. Besides, stable resistance retention exceeding 3.4×10^4 s and a large memory window (on/off ratio) up to 10^3 is achieved by applying a continuous bias of 0.1 V, as shown in Fig. 3(e). The time-dependent stability of the Pt/MoS_2@LCO_{35}-PVA/Si dendritic memristor is assessed for 10-day intervals, as shown in Fig. 3(f). The changes in the *I-V* curves are minimal, confirming the stable environmental memristive properties. The consecutive cycles of the memristors with LCO concentrations of 0 wt%, 10 wt%, and 50 wt% are shown in Figs. S5(a)-(c), and the corresponding endurance properties are shown in Figs. S5(d)-(f). The coefficients of variation (C_v) are statistically determined as shown in Table S1 to evaluate device stability. According to Formula (1):

$$C_V = \frac{\sigma}{\mu} \tag{1}$$

where σ is the standard deviation and μ is the mean. The 35 wt% LCO sample shows smaller C_v in both HRS and LRS of approximately 0.26 and 0.63, respectively. The statistical errors for the SET voltage (V_{SET}) in Fig. 3 (g) show that the voltage variation of the 35 wt% sample (σ = 0.20) is smaller than those of the 10 wt% sample (σ = 0.37) and 50 wt% sample (σ = 0.35). The improved cycling stability and reduced variability in the switching voltage of MoS_2@LCO_{35}-PVA based memristor can be attributed to the synergistic effect of the dendritic structure and embedded MoS_2 nanosheets, leading to less randomness of the conductive channels. The device-to-device variation is analyzed by scanning the voltage from −3 V to 2 V using a voltage step of ± 0.01 V and I_{cc} of 10 mA, respectively, as shown in Fig. S6(a). *I-V* curves of 10 devices are compared and the characteristics of the *I-V* curves are similar to Fig. 3(c). The HRS and LRS values with 10 devices are statistically investigated, the C_v of HRS and LRS of the device is 0.36 and 0.31, respectively, as shown in Fig. S6(b). Moreover, Fig. 3 (h) compares the SET voltage and endurance properties of MoS_2@LCO_{35}-PVA with those of other similar synaptic memristors reported in the literature. The MoS_2@LCO_{35}-PVA dendritic memristor has better properties and is capable of operating at lower switching voltages with excellent DC voltage sweep endurance. The structure and corresponding memristive properties are summarized in Table S2.

The conductive mechanism of the MoS_2@LCO_{35}-PVA dendritic memristor is analyzed by replotting the log(*I*)-log(|*V*|) curves for SET and RESET progress, as shown in Fig. 4(a). During the SET progress, the switching behavior fits that of the classical trap-controlled space charge limited current model, expressed as $I = \beta V^{\alpha}$, where β and α represent the constant and the exponential index, respectively [34,35]. Fig. 4(a-I) show that the SET process is segmented into three distinct voltage regions. In the low voltage region (0 V to 0.19 V), a slope of 1.16 (close to 1) indicates an Ohmic region controlled by thermally excited carriers. The slope of the high voltage region (0.2 V to 0.8 V) is 2.07 and follows the trap-filled space charge limited current ($\alpha \approx 2$). When the applied voltage reaches the threshold voltage (V_{th}) of 0.82 V, β is fitted to be 8.38, marking a steep increase in the current as the device transitions from the HRS to LRS. In LRS, the observed slope of 1.02 suggests Ohmic conduction, indicating that Li^+ ions interact with MoS_2 nanosheets and are stored stably, resulting in the 2H-1T phase transition to form conductive channels. On the contrary, Li^+ ions begin to migrate back

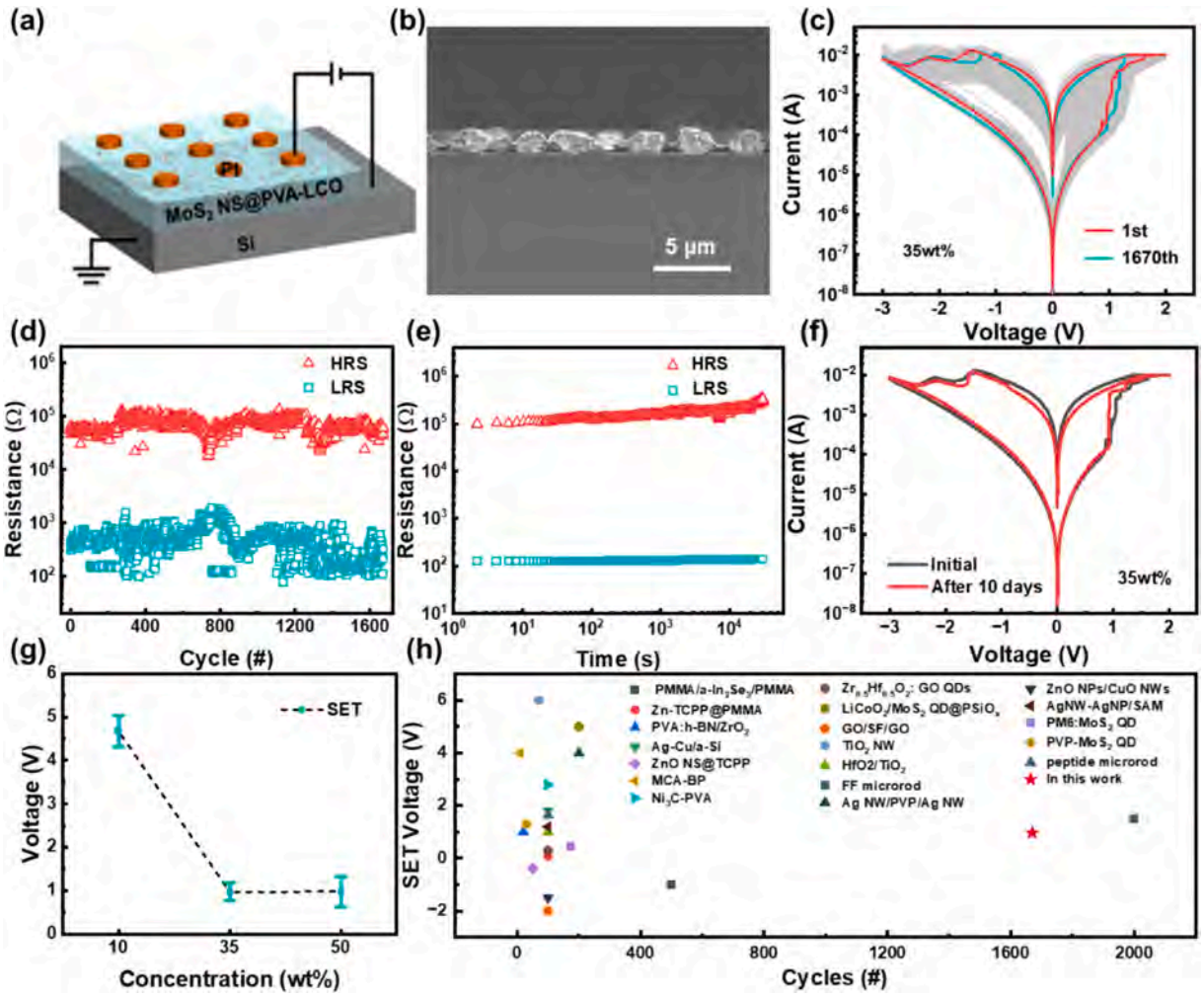

Fig. 3. (a) Schematic of the Pt/MoS_2@LCO-PVA/Si memristor; (b) Cross-sectional SEM image of the Pt/MoS_2@LCO-PVA/Si stack; (c) *I-V* characteristics of the Pt/MoS_2@LCO-PVA/Si dendritic device; (d) Endurance assessment; (e) Retention time of the MoS_2@LCO_{35}-PVA dendritic memristor; (f) *I-V* curves of the MoS_2@LCO_{35}-PVA dendritic memristor for a 10-day interval; Statistical analysis of (g) SET voltages for various LCO mass fractions; (h) Comparison of switching cycles and SET voltages of the MoS_2@LCO-PVA dendritic memristor with those of other microstructures such as quantum dots, nanosheets, nanoclusters, nanowires, and microrods.

after the voltage reaches V_{th} of –1.36 V as shown in Fig. 4(a-II), causing a rupture of the conductive channel in the conductive region during the RESET progress. As the voltage is scanned from –3.00 V to –0.22 V, trapped electrons are released gradually showing slopes of 3.53 and 2.22, respectively. The current is mainly generated by thermal excitation, and the device switches from the LRS to the HRS with a slope of 1.14 at voltages between –0.22 V and 0 V.

COMSOL Multiphysics simulation is performed to analyze the electric field distribution in the MoS_2@LCO_{35}-PVA dendritic memristor. Fig. 4(b-I) shows that a local enhanced electric field (~10^7 V/cm) is observed at the interface between the dendritic structure and Si substrate, compared to the without dendritic structure in Fig. S7, which can constrain the transport of ions laterally. Furthermore, a significant enhancement near the MoS_2 nanosheets in the resistive layer, reaching about 5×10^6 V/cm, as shown in Fig. 4(b-II). Under the electric field, Li^+ ions accumulate around the MoS_2 nanosheets and undergo electrochemical reactions. Fig. 4(c) depicts the HR-TEM images of the MoS_2 nanosheets, where Mo and S atoms are represented by solid red and blue circles, respectively. The presence of S vacancies (V_S) and Mo vacancies (V_{Mo}) is confirmed by analyzing the integrated pixel intensity profiles in the orange solid box in Fig. 4(c). And a significant decline in the line intensity is observed in Fig. 4(d) [36,37]. Fig. 4(e) is the X-ray photoelectron spectroscopy (XPS) analysis of the high-resolution Mo 3*d* core level spectra and Mo^{3+} peaks located at 229.05 eV ($3d_{5/2}$) and 232.15 eV ($3d_{3/2}$), Mo^{4+} peaks at 229.75 eV ($3d_{5/2}$) and 232.85 eV ($3d_{3/2}$), Mo^{5+} peaks at 230.05 eV ($3d_{5/2}$) and 233.45 eV($3d_{3/2}$) as well as Mo^{6+} peaks at 234.65 eV($3d_{5/2}$) and 236.45 eV($3d_{3/2}$). The Mo^{3+} and Mo^{5+}/Mo^{6+} peaks confirm the presence of V_{Mo} and V_S in the MoS_2 nanosheets, which provide abundant electrochemically active sites to trap Li^+ ions [38,39], leading to a long retention time and high reversible cycling. The underlying memristive mechanism is illustrated in Fig. S8. Figs. S8(a)-(c) show the schematic diagram of the memristive mechanism in the Pristine state, SET, and RESET process, respectively. Fig. S8(a) is the Pristine state with no electric field and vacancies are distributed in MoS_2 nanosheets. In the SET process [Fig. S8(b)], a positive voltage is applied, Li^+ ions are extracted from LCO and reacted with MoS_2 nanosheets due to the presence of electrochemically active sites. As the concentration of Li^+ ions gradually increases, the MoS_2 nanosheets transition from the 2H phase to the 1 T phase, forming conductive paths that cause the device to exhibit an LRS [29,30]. In the RESET process [Fig. S8(c)], a negative voltage is applied and Li^+ ions de-intercalate from MoS_2 nanosheets. The conductive paths break down and the resistive state changed from LRS to HRS. The electrochemical reaction in the memristive process is:

$$mLi^+ + MoS_2 + me^- \leftrightarrow Li_mMoS_2. \quad (2)$$

Synaptic plasticity is an important factor in NC applications and various synaptic plasticity behaviors are simulated, as shown in Fig. 5. Fig. 5(a) shows that the information is transmitted from the pre-synaptic

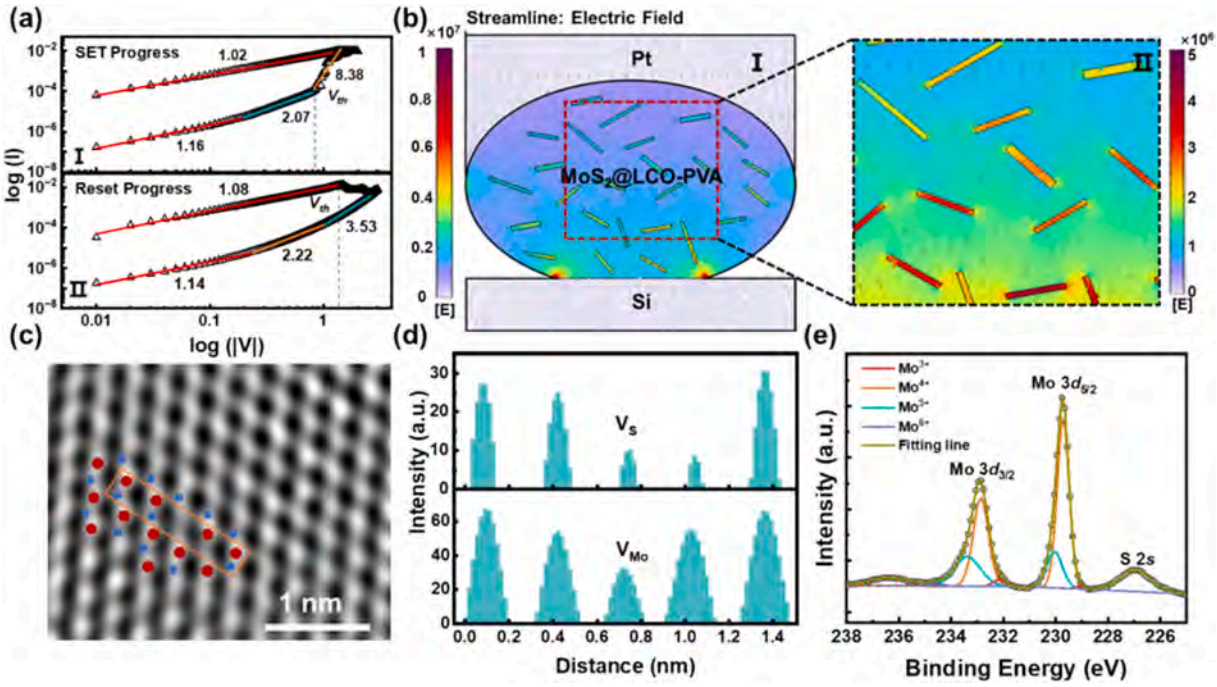

Fig. 4. Mechanistic analysis of the Pt/MoS_2@LCO-PVA/Si dendritic memristor: (a) Fitted log(I)-log($|V|$) curve of the MoS_2@LCO-PVA dendritic-based device, indicating a memristive process governed by space charge limited currents; (b) Electric field simulation of the device using the COMSOL Multiphysics software; (c) TEM images of MoS_2 nanosheets; (d) Line profiles of Mo and S; (e) Mo 3d spectrum of MoS_2 nanosheets in the MoS_2@LCO_{35}-PVA dendritic structure.

to post-synaptic neurons by external stimulation. The synaptic weight represents the strength of the signal connection between two neurons, and the change in the conductance indirectly reflects the synaptic weight of the device. Fig. 5(b) and 5(c) display the corresponding voltage-time (V-t) and current-time (I-t) curves, showing that the gradual regulation of conductance is realized by employing a triangular waveform. The synaptic connection is progressively strengthened through five consecutive positive voltage sweeps (0 V → 0.6 V → 0 V), as shown in Fig. 5(b). Conversely, Fig. 5(c) shows synaptic depression when the device is subjected to five consecutive negative voltage scans (0 V → –1.6 V → 0 V). Fig. 5(d) shows three cycles of long-term potentiation (LTP) and long-term depression (LTD) behaviors of the device, demonstrating the reliability of these cycles. The LTP and LTD properties, induced by pulse signal regulation, are measured using 20 positive pulses of 1 V and 20 negative pulses of –1 V, each with a 5 ms pulse width. The conductance of synaptic device increases with the application of positive pulses and decreases with negative pulses. To further evaluate device stability, a single pulse with different pulse amplitudes (1.5 V, 2.0 V, 2.2 V, 2.5 V, and 3 V; pulse width 500 ms) are used to modulate the conductance states and the conductance states gradually increases from 13 μS to 1046 μS which can be stable for 10 s, as shown in Fig. 5(e). In biological neural networks, information can be processed and stored by adjusting the pulse amplitude, interval and width to simulate changes in the synaptic weight. Fig. 5(f)-(h) show the effects of different pulse amplitudes (1 V, 2 V, and 3 V), pulse intervals (3 ms, 5 ms, and 7 ms) and pulse width (3 ms, 5 ms, and 7 ms) on the synaptic weight, respectively. As the amplitude increases, pulse interval decreases and the pulse width increases, the changes in the synaptic weight become more pronounced due to the enhanced interaction between Li^+ ions with MoS_2 nanosheets. The change in the synaptic weight is described by the following equation:

$$W\% = \left(\frac{G_n - G_0}{G_0}\right) \times 100\% \quad (3)$$

where G_0 represents the initial conductance state and G_n (n = 1,2,3, … 20) is the corresponding conductance after stimulation. Energy efficiency plays an important role in the practical application of artificial synapses. The energy consumption for a single electrical pulse (pulse amplitude 1 V, pulse width 5 ms) can be calculated based on the integration of current over applying pulse time, as shown in Fig. S9. Since the energy consumption is proportional to the effective device area [40], the areal energy consumption in the dendritic MoS_2@LCO-PVA device is 0.56 fJ/um^2, demonstrating a superior performance compared to most reported devices (such as those with different microstructural and Li^+ ions based synaptic devices), as shown in Table S3. Spike timing-dependent plasticity (STDP) is one of the advanced learning rules in the biological brain for competitive Hebbian learning. The synaptic weight can be adjusted by changing the time intervals between pre-synaptic and post-synaptic spikes. To verify the STDP learning rule, pulse pairs with different time intervals from 10 ms to 90 ms and pulse amplitude of 2 V/–2 V are applied to the MoS_2@LCO_{35}-PVA dendritic memristor, as shown in Fig. 5(i). Fig. 5(j) indicates the STDP behavior with respect to the change in the synaptic weight (ΔW) versus time interval (Δt), which is consistent with the antisymmetric Hebbian learning rule. When the pre-synaptic pulse precedes the post-synaptic pulse ($\Delta t > 0$), the synaptic weight increases, leading to the LTP of the device. On the contrary, when the pre-synaptic pulse follows the post-synaptic pulse ($\Delta t < 0$), the synaptic weight decreases to convert the device to LTD. The red and blue circles in Fig. 5(j) are fitted with the following exponential function:

$$\Delta W = A\exp\left(\frac{\Delta t}{\tau_{\pm}}\right) + W_0 \quad (4)$$

where "+" represents $\Delta t > 0$, "–" represents $\Delta t < 0$, and A and τ (τ_+, τ_-) are the scaling factor and time constant of the STDP learning rule, respectively. Here, $\tau_+ = 9.56$ ms and $\tau_- = 3.89$ ms in the STDP learning rule, consistent with the time constant of the STDP window of a biological synapse.

The artificial neural network (ANN) is developed to perform supervised learning on the MNIST handwritten digit dataset using the Back-propagation algorithm [41]. Fig. 6(a) illustrates the schematic of the ANN simulation, which features an input layer with 28 × 28 neurons, a

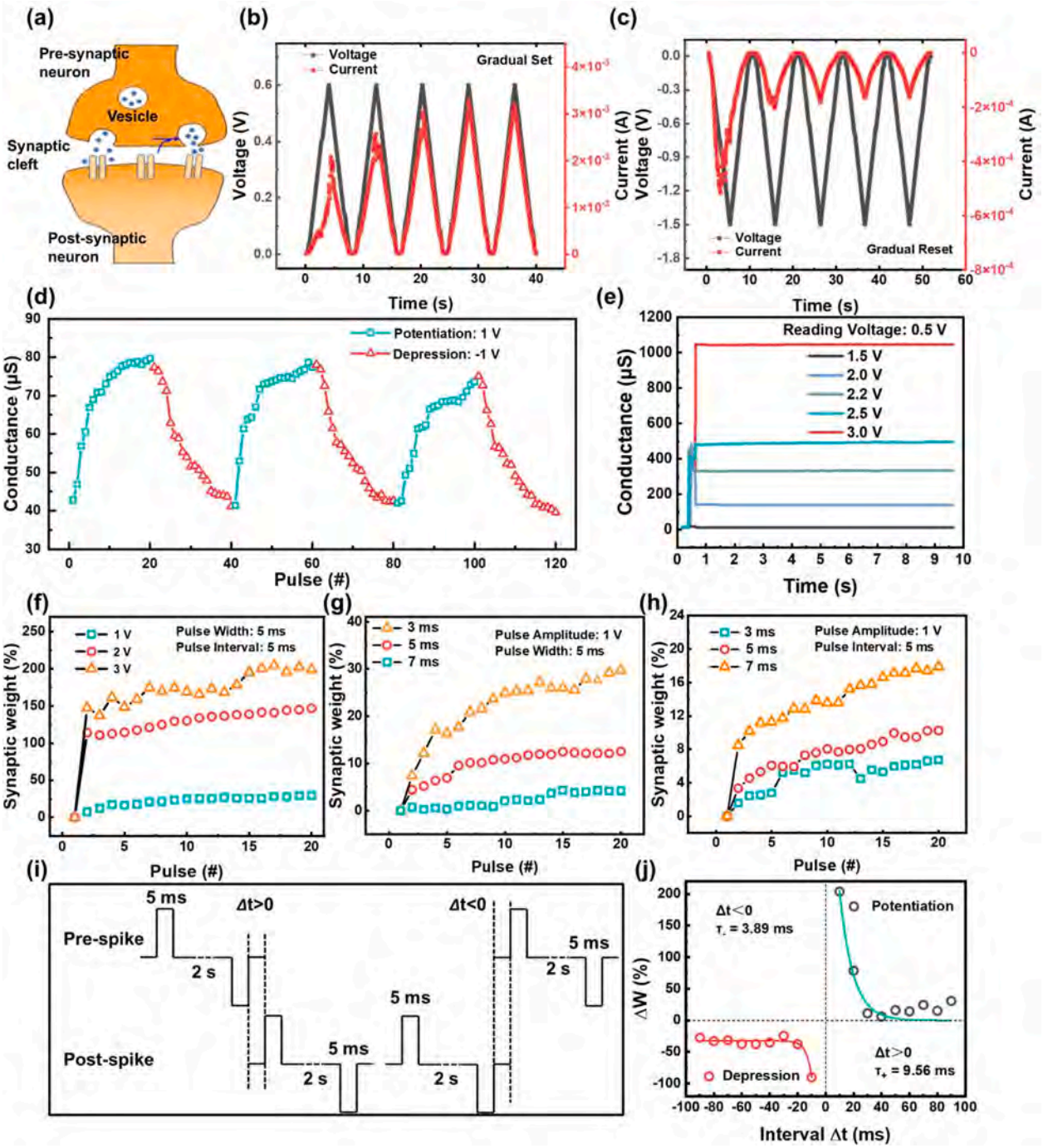

Fig. 5. (a) Biological synapse schematic; (b) Gradual setting of the MoS_2@LCO_{35}-PVA-based dendritic device under consecutive positive sweeping voltages (0 V → +0.6 V → 0 V); (c) Gradual resetting under negative sweeping voltages (0 V → –1.6 V → 0 V); (d) Stable LTP/LTD characteristics realized by applying 20 continuous 1 V pulses and −1 V pulses with time width of 5 ms; (e) Nonvolatile of conductance states during the LTP by regulating different pulse voltage amplitudes (1.5 V, 2.0 V, 2.2 V, 2.5 V and 3.0 V); (f) Pulse amplitude (5 ms width and 5 ms interval); (g) Pulse intervals (1 V amplitude, 5 ms width); (h) Pulse widths (1 V amplitude, 5 ms interval); (i)-(j) Measurement conditions of STDP and corresponding simulation results according to the asymmetric Hebbian rule, where the circles represent experimental data and the solid line is the fitted curve.

hidden layer comprising 100 neurons, and an output layer with 10 neurons. The conductance changes in Fig. 6(b) represent the synaptic weight updates essential for pattern recognition and the crossbar array is composed of MoS_2@LCO_{35}-PVA dendritic memristors, as illustrated in Fig. 6(c). In each training step, 50 images are randomly selected from the MNIST dataset containing 6×10^4 handwritten digital images for training the ANN. A high recognition accuracy of 91.4 % based on the real device performance is achieved after 7,200 training steps (6 epochs) and is comparable to the 93.4 % recognition accuracy obtained by simulating an ideal synaptic device, as shown in Fig. 6(c). The confusion matrix of the MoS_2@LCO_{35}-PVA dendritic synaptic memristors after 50, 1,200, and 7,200 training steps is presented in Fig. 6(d)-(f). The matrix transforms from chaos to standard as the training steps increase, thereby revealing the significant potential of MoS_2@LCO_{35}-PVA dendritic synaptic memristor for information processing in MNIST pattern recognition.

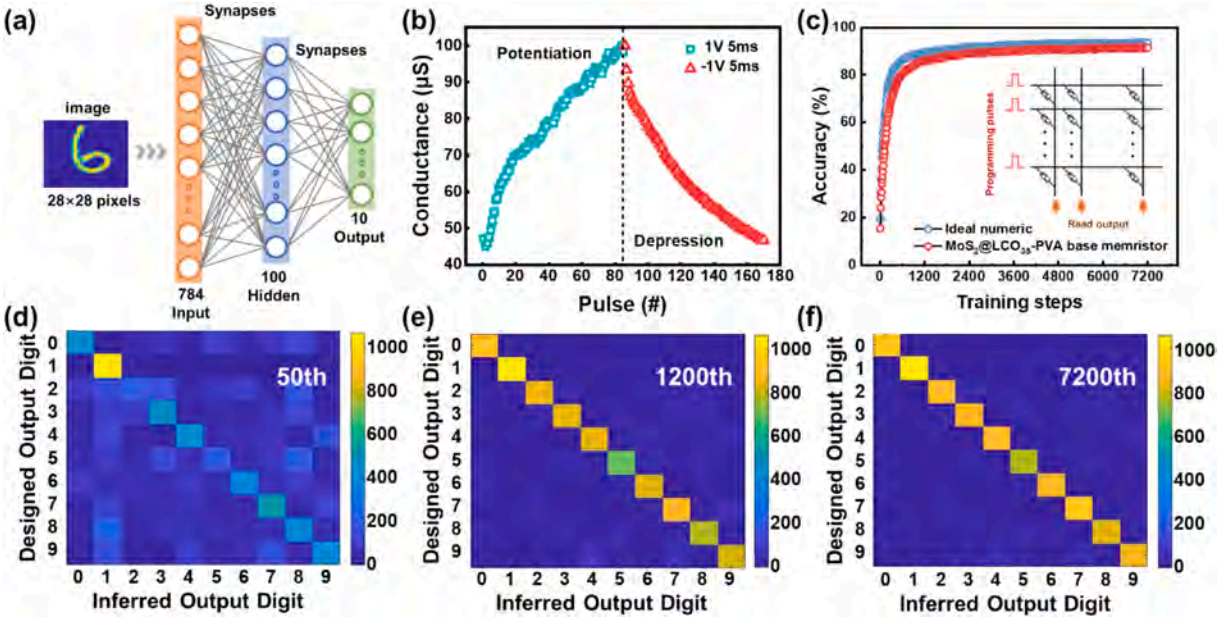

Fig. 6. (a) Schematic of the three-layer neural network for handwritten digit recognition; (b) LTP/LTD characteristics realized by applying 85 continuous 1 V pulses and −1 V pulses with time width of 5 ms; (c) Recognition accuracy of the experimental and ideal synaptic devices; Confusion matrices for training results: (d) 50th training steps, (e) 1200th training steps, and (f) 7200th training steps. The corresponding digit is recognized successfully when a large value appears along the diagonal line.

3. Conclusions

A functionalized dendritic synaptic memristor with the Pt/MoS_2@LCO_{35}-PVA/Si structure is fabricated and stable memristive characteristics are achieved. The mechanism of the memristive properties is analyzed and discussed based on the ion kinetics. The typical synaptic plasticity is simulated, and the device achieves a high level of accuracy in image recognition of 91.4 %. These results provide insights and guidance into the development of accurate pattern recognition for NC.

4. Experimental Section

4.1. Materials

PVA (average mol M_w = 30,000–70,000) was purchased from Beijing InnoChem Science &Technology Co., Ltd. The liquid-phase exfoliation MoS_2 dispersion solution (0.05 μm-1 μm, 1–10 layers) was obtained from Nanjing MKNANO Tech. Co., Ltd. And $LiClO_4{\cdot}3H_2O$ (AR, 99.0 %) was bought from Shanghai Aladdin Bio-Chem Technology Co., Ltd.

4.2. Preparation of MoS_2@LCO-PVA solution

A 5 wt% water-soluble PVA was used as the polymer matrix, which was mixed with deionized water and stirred at 90 ℃ for 2 h to ensure complete dissolution. $LiClO_4{\cdot}3H_2O$ with different mass fractions (0, 10, 35, and 50 wt%) and MoS_2 nanosheets with a concentration of 2 wt% were introduced to the PVA solution. The resultant MoS_2@LCO-PVA solution was stirred at room temperature for 6 h to achieve full dispersion.

4.3. Preparation of Pt/MoS_2@LCO-PVA/Si device

The highly-doped p-type Si (100) wafer was sequentially ultrasonically cleaned in acetone, absolute ethanol, and deionized water for 15 min each, and then dried under a nitrogen flow at room temperature. Subsequently, the MoS_2@LCO-PVA nanocomposite solution was spin-coated onto the Si substrate at 500 rpm for 10 s and 5,000 rpm for 50 s to prepare the MoS_2@LCO-PVA structure. A circular Pt top electrode with a diameter of 500 μm was sputter-deposited onto the MoS_2@LCO-PVA layer by DC magnetron sputtering using a shadow mask.

4.4. Characterization

The morphology and elemental composition of the samples were characterized by optical microscopy, scanning electron microscopy (SEM, ZEISS Gemini SEM 300), and energy-dispersive X-ray spectroscopy (EDS). The crystal structure of the MoS_2 nanosheets was examined by high-resolution transmission electron microscopy (HR-TEM, JEM2100). X-ray photoelectron spectroscopy and Raman scattering were performed on the Esca Lab 250Xi and Nanofinder® 30, respectively. The electrical measurements were carried out on the Keithley 4200-SCS semiconductor parametric analyzer and AFG31000 Series Arbitrary Function Generator.

4.5. Pattern recognition simulation

The circuit simulation of artificial neural networks (ANNs) is conducted using Matlab 2023b. The simulation is based on the backpropagation algorithm, utilizing experimental long-term synaptic plasticity (LTP, LTD) characteristics. A three-layer fully connected neural network, consisting of 784 input neurons, 100 hidden neurons, and 10 output neurons, are employed. The network is trained using 60,000 MNIST images (28 × 28 pixels) of handwritten digits (0-9) with the backpropagation algorithm, while a separate MNIST dataset of 10,000 handwritten digits is used for testing the recognition accuracy. To reduce the writing frequency of the device, the network is updated after randomly inputting 50 images, with the updated weights written into the device array. Each weight update is defined as a step.

CRediT authorship contribution statement

Xueli Geng: Writing – original draft, Data curation. **Qin Gao:** Writing – review & editing. **Jiangshun Huang:** Methodology. **Juan Gao:** Supervision. **Pengzhan Li:** Formal analysis. **Yihang Liu:** Supervision. **Qiaofeng Yang:** Supervision. **Xinghe Li:** Supervision. **Hao**

Zhang: Funding acquisition. **Zhisong Xiao:** Supervision. **Mei Wang:** Supervision. **Paul K. Chu:** Funding acquisition. **Anping Huang:** Supervision, Funding acquisition.

Declaration of competing interest

The authors declare that they have no known competing financial interests or personal relationships that could have appeared to influence the work reported in this paper.

Acknowledgments

This research was supported by the National Natural Science Foundation of China (Grant Nos. 52403315 and 52473251), Industry University Research Cooperation Fund of the Eighth Research Institute of China Aerospace Science and Technology Corporation (SAST2023-030), the National Key Research and Development Program of China (Grant No.2021YFB3900701) and City University of Hong Kong Donation Research Grant (Grant Nos. DON-RMG 9229021 and 9220061).

Appendix A. Supplementary data

Supplementary data to this article can be found online at https://doi.org/10.1016/j.cej.2025.161487.

Data availability

Data will be made available on request.

References

[1] K. Roy, A. Jaiswal, P. Panda, Towards Spike-Based Machine Intelligence with Neuromorphic Computing, *Nature* 575 (2019) 607–617.
[2] J. Yan, J.P.K. Armstrong, F. Scarpa, A.W. Perriman, Hydrogel-Based Artificial Synapses for Sustainable Neuromorphic Electronics, *Adv. Mater.* 36 (2024) 2403937.
[3] X. Duan, Z. Cao, K. Gao, W. Yan, S. Sun, G. Zhou, Z. Wu, F. Ren, B. Sun, Memristor-Based Neuromorphic Chips, *Adv. Mater.* 36 (2024) 2310704.
[4] S.H. Jo, T. Chang, I. Ebong, B.B. Bhadviya, P. Mazumder, W. Lu, Nanoscale Memristor Device as Synapse in Neuromorphic Systems, *Nano Lett.* 10 (2010) 1297–1301.
[5] A. Sebastian, M. Le Gallo, R. Khaddam-Aljameh, E. Eleftheriou, Memory Devices and Applications for in-Memory Computing, *Nat. Nanotechnol.* 15 (2020) 529–544.
[6] W. Zhang, Y. Chen, C. Xu, C. Lin, J. Tao, Y. Lin, J. Li, O.V. Kolosov, Z. Huang, Tunable Electrical Field-Induced Metal-Insulator Phase Separation in $LiCoO_2$ Synaptic Transistor Operating in Post-Percolation Region, *Nano Energy* 108 (2023) 108199.
[7] Y. Chen, W. Zhang, Y. Lu, M. Chen, J. Chen, H. Lu, Y. Nie, G. Zhao, J. Tao, J. Li, Y. Lin, O. Kolosov, Z. Huang, Inhibiting the Current Spikes within the Channel Layer of $LiCoO_2$-based Three-terminal Synaptic Transistors, *Appl. Phys. Rev.* 11 (2024) 041407.
[8] Y. Zhang, G.Q. Mao, X. Zhao, Y. Li, M. Zhang, Z. Wu, W. Wu, H. Sun, Y. Guo, L. Wang, X. Zhang, Q. Liu, H. Lv, K.-H. Xue, G. Xu, X. Miao, S. Long, M. Liu, Evolution of the Conductive Filament System in HfO_2-Based Memristors Observed by Direct Atomic-Scale Imaging, *Nat. Commun.* 12 (2021) 7232.
[9] C. Yang, H. Wang, Z. Cao, X. Chen, G. Zhou, H. Zhao, Z. Wu, Y. Zhao, B. Sun, Memristor-Based Bionic Tactile Devices: Opening the Door for Next-Generation Artificial Intelligence, *Small* 20 (2024) 2308918.
[10] Z. Wang, H. Wu, G.W. Burr, C.S. Hwang, K.L. Wang, Q. Xia, J.J. Yang, Resistive Switching Materials for information Processing, *Nat. Rev. Mater.* 5 (2020) 173–195.
[11] Y. Li, L. Loh, S. Li, L. Chen, B. Li, M. Bosman, K.W. Ang, Anomalous Resistive Switching in Memristors Based on Two-Dimensional Palladium Diselenide Using Heterophase Grain Boundaries, *Nat. Electron.* 4 (2021) 348–356.
[12] W. Chen, Z. Mou, Y. Xin, H. Li, T. Wang, Y. Chen, L. Chen, B.R. Yang, Z. Chen, Y. Luo, G.-S. Liu, Self-Assembled Monolayer and Nanoparticles Coenhanced Fragmented Silver Nanowire Network Memristor, *ACS Appl. Mater. Interfaces* 16 (2024) 6057–6067.
[13] Q. Zhang, Q. Jiang, F. Fan, G. Liu, Y. Chen, B. Zhang, MoS_2 Quantum Dot-Optimized Conductive Channels for a Conjugated Polymer-Based Synaptic Memristor, *ACS Appl. Mater. Interfaces* 15 (2023) 59630–59642.
[14] C. Yeon, S.J. Yun, J. Yang, D.H. Youn, J.W. Lim, Na-Cation-Assisted Exfoliation of MX_2 (M = Mo, W; X = S, Se) Nanosheets in an Aqueous Medium with the Aid of a Polymeric Surfactant for Flexible Polymer-Nanocomposite Memory Applications, *Small* 14 (2017) 1702747.
[15] X. Zhang, C. Wu, Y. Lv, Y. Zhang, W. Liu, High-Performance Flexible Polymer Memristor Based on Stable Filamentary Switching, *Nano Lett.* 22 (2022) 7246–7253.
[16] B.M. Lim, Y.M. Lee, C.S. Yoo, M. Kim, S.J. Kim, S. Kim, J.J. Yang, H.S. Lee, High-Reliability and Self-Rectifying Alkali Ion Memristor through Bottom Electrode Design and Dopant Incorporation, *ACS Nano* 18 (2024) 6373–6386.
[17] T. Sun, F. Yu, X. Tang, H. Li, F. Zhang, Z. Xu, Q. Liao, Z. Yu, X. Liu, P. Wangyang, H. Li, Y. Peng, Organic-2D Composite Material-Based Rram with High Reliability for Mimicking Synaptic Behavior, *J. Materiomics* 10 (2024) 440–447.
[18] X. Yan, L. Zhang, H. Chen, X. Li, J. Wang, Q. Liu, C. Lu, J. Chen, H. Wu, P. Zhou, Graphene Oxide Quantum Dots Based Memristors with Progressive Conduction Tuning for Artificial Synaptic Learning, *Adv. Funct. Mater.* 28 (2018) 1803728.
[19] H.C. Lee, J. Kim, H.R. Kim, K.H. Kim, K.J. Park, J.P. So, J.M. Lee, M.S. Hwang, H. G. Park, Nanograin Network Memory with Reconfigurable Percolation Paths for Synaptic Interactions, *Light Sci. Appl.* 12 (2023) 118.
[20] Q. Lu, F. Sun, L. Liu, L. Li, Y. Wang, M. Hao, Z. Wang, S. Wang, T. Zhang, Biological Receptor-Inspired Flexible Artificial Synapse Based on Ionic Dynamics, *Microsyst. Nanoeng.* 6 (2020) 84.
[21] H. Liu, Q. Hua, R. Yu, Y. Yang, T. Zhang, Y. Zhang, C. Pan, A Bamboo-Like GaN Microwire-Based Piezotronic Memristor, *Adv. Funct. Mater.* 26 (2016) 5307–5314.
[22] Y. Liu, X. Zhou, H. Yan, X. Shi, K. Chen, J. Zhou, J. Meng, T. Wang, Y. Ai, J. Wu, J. Chen, K. Zeng, L. Chen, Y. Peng, X. Sun, P. Chen, H. Peng, Highly Reliable Textile-Type Memristor by Designing Aligned Nanochannels, *Adv. Mater.* 35 (2023) 2301321.
[23] Q. Gao, J. Huang, J. Gao, X. Geng, Y. Ji, H. Li, G. Wang, B. Liang, M. Wang, Z. Xiao, Y. Zhu, P.K. Chu, A. Huang, Tunable Plasticity in Functionalized Honeycomb Synaptic Memristor for Neurocomputing, *Mater. Today Phys.* 30 (2023) 100947.
[24] J. Zhang, W. Liu, J. Dai, K. Xiao, Nanoionics from Biological to Artificial Systems: An Alternative Beyond Nanoelectronics, *Adv. Sci.* 9 (2022) 2200534.
[25] Q. Gao, A. Huang, J. Zhang, Y. Ji, J. Zhang, X. Chen, X. Geng, Q. Hu, M. Wang, Z. Xiao, P.K. Chu, Artificial Synapses with a Sponge-Like Double-Layer Porous Oxide Memristor, *NPG Asia Mater.* 13 (2021) 3.
[26] X. Geng, Q. Gao, G. Wu, J. Huang, G. Wang, Y. Xin, J. Gao, B. Liang, L. Gao, M. Wang, Z. Xiao, P.K. Chu, A. Huang, Stable and Tunable Quantum Conductance in Spider-Silk-Like Synaptic Device for Neurocomputing, *ACS Appl. Mater. Interfaces* 16 (2024) 39807–39817.
[27] Du, W.; Shen, K.; Qi, Y.; Gao, W.; Tao, M.; Du, G.; Bao, S. j.; Chen, M.; Chen, Y.; Xu, M. Efficient Catalytic Conversion of Polysulfides by Biomimetic Design of "Branch-Leaf" Electrode for High-Energy Sodium-Sulfur Batteries. *Nano-Micro Letters* **2021**, *13*, 50.
[28] P. Yang, Z. Wu, Y. Jiang, Z. Pan, W. Tian, L. Jiang, L. Hu, Fractal $(Ni_xCo_{1-X})_9Se_8$ Nanodendrite Arrays with Highly Exposed (011) Surface for Wearable, All-Solid-State Supercapacitor. *Advanced Energy Materials* 8 (2018) 1801392.
[29] X. Zhu, D. Li, X. Liang, W.D. Lu, Ionic Modulation and Ionic Coupling Effects in MoS_2 Devices for Neuromorphic Computing, *Nat. Mater.* 18 (2018) 141–148.
[30] M. Xie, Z. Lv, W. Zhao, Y. Fang, J. Huang, F. Huang, Intercalated Hydrates Stabilize Bulky MoS_2 Anode for Lithium-Ion Battery, *Chem. Eng. J.* 470 (2023) 144282.
[31] S.K. Kim, J.J. Wie, Q. Mahmood, H.S. Park, Anomalous Nanoinclusion Effects of 2D MoS_2 and WS_2 Nanosheets on the Mechanical Stiffness of Polymer Nanocomposites, *Nanoscale* 6 (2014) 7430–7435.
[32] H.F. Rouhi, H.M. Chenari, Two-Dimensional (2D) MoS_2-Nanosheet (NS) Incorporated within Electrospun PVA Nanofibers: Fabrication and Characterization Study, *Surf. Interfaces* 51 (2024) 104702.
[33] T. Livneh, E. Sterer, Resonant Raman Scattering at Exciton States Tuned by Pressure and Temperature in 2H-MoS_2, *Phys. Rev. B* 81 (2010) 195209.
[34] M. Xiao, K.P. Musselman, W.W. Duley, N.Y. Zhou, Resistive Switching Memory of TiO_2 Nanowire Networks Grown on Ti Foil by a Single Hydrothermal Method, *Nano-Micro Letters* 9 (2016) 15.
[35] Y.H. Ji, A.P. Huang, M.Q. Yang, Q. Gao, X.L. Yang, X.L. Chen, M. Wang, Z.S. Xiao, R.Z. Wang, P.K. Chu, Wrinkled-Surface-Induced Memristive Behavior of MoS_2 Wrapped Gan Nanowires, *Adv. Electron. Mater.* 6 (2020) 2000571.
[36] Y. Shi, J. Li, C. Mao, S. Liu, X. Wang, X. Liu, S. Zhao, X. Liu, Y. Huang, Z.L. Van Der, Waals Gap-Rich BiOCl Atomic Layers Realizing Efficient, Pure-Water CO_2-to-CO Photocatalysis, *Nat. Commun.* 12 (2021) 5923.
[37] X. Yan, Q. Zhao, A.P. Chen, J. Zhao, Z. Zhou, J. Wang, H. Wang, L. Zhang, X. Li, Z. Xiao, K. Wang, C. Qin, G. Wang, Y. Pei, H. Li, D. Ren, J. Chen, Q. Liu, Vacancy-Induced Synaptic Behavior in 2D WS_2 Nanosheet-Based Memristor for Low-Power Neuromorphic Computing, *Small* 15 (2019) 1901423.
[38] Y. Liu, L. Zhang, Y. Zhao, T. Shen, X. Yan, C. Yu, H. Wang, H. Zeng, Novel Plasma-Engineered MoS_2 Nanosheets for Superior Lithium-Ion Batteries, *J. Alloy. Compd.* 787 (2019) 996–1003.
[39] Ma, X.; Diao, L.; Wang, Y.; zhang, L.; Lu, Y.; Li, D.; Yang, D.; She, X. Vacancies Manipulating Enhances Na^+ Insertion of MoS_2 for Efficient Sodium-Ion Storage. *Chemical Engineering Journal* **2023**, *457*, 141116.
[40] Y. van de Burgt, E. Lubberman, E. Fuller, S.T. Keene, G.c. Faria, S. Agarwal, M. J. Marinella, A.A. Talin, A. Salleo, A non-volatile organic electrochemical device as a low-voltage artificial synapse for neuromorphic computing, *Nat. Mater.* 16 (2017) 414–418.
[41] S. Choi, S.H. Tan, Z. Li, Y. Kim, C. Choi, P.Y. Chen, H. Yeon, S. Yu, J. Kim, SiGe Epitaxial Memory for Neuromorphic Computing with Reproducible High Performance Based on Engineered Dislocations, *Nat. Mater.* 17 (2018) 335–340.

Functionalized Dendritic Memristor of Pt/MoS_2@LCO-PVA/Si for Mimicking Synaptic Behavior

Xueli Geng[1], Qin Gao[2*], Jiangshun Huang[1], Juan Gao[1], Pengzhan Li[1], Yihang Liu[1], Qiaofeng Yang[1], Xinghe Li[1], Hao Zhang[3], Zhisong Xiao[1&2], Mei Wang[1], Paul K. Chu[4], Anping Huang[1*]

[1] *School of Physics, Beihang University, Beijing 100191, China*

[2] *School of Applied Science, Beijing Information Science & Technology University, Beijing 102206, China*

[3] *School of Space and Earth Sciences, Beihang University, Beijing 100191, China*

[4]*Department of Physics, Department of Materials Science and Engineering, and Department of Biomedical Engineering, City University of Hong Kong, Tat Chee Avenue, Kowloon, Hong Kong, China*

* Corresponding Author: gaoqin@bistu.edu.cn; aphuang@buaa.edu.cn; Tel: 86-10-61716876; Fax: 86-10-61716876

1. Optical images of PVA-LCO structure.

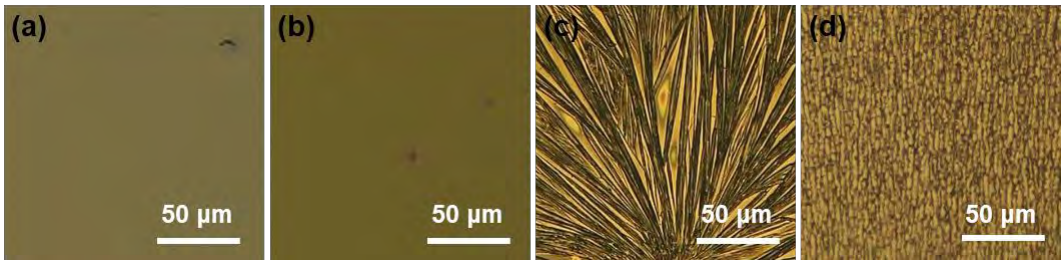

Figure S1. Optical images of PVA-LCO structures with different LCO doping concentrations: (a) 0 wt%, (b) 10 wt%, (c) 35 wt% and (d) 50 wt%.

2. The *I-V* curves of Pt/LCO-PVA/Si devices.

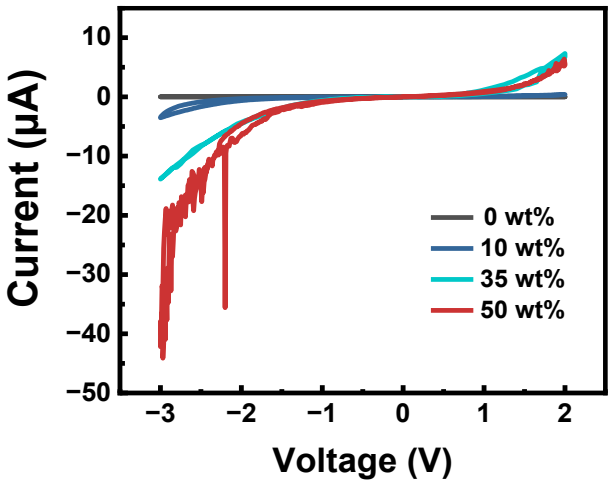

Figure S2. *I-V* curves of Pt/LCO-PVA/Si devices with different LCO doping concentrations of 0 wt%, 10 wt%, 35 wt%, and 50 wt%.

3. SEM images of MoS_2@PVA-LCO structure.

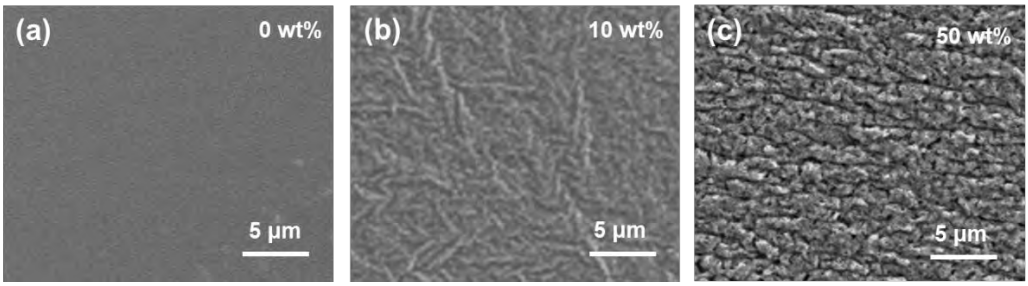

Figure S3. SEM images of MoS_2@PVA-LCO structures with different LCO doping concentrations: (a) 0 wt%, (b) 10 wt%, and (c) 50 wt%.

4. Atomic force microscope (AFM) characterization of MoS_2@PVA-LCO thin films with different concentrations.

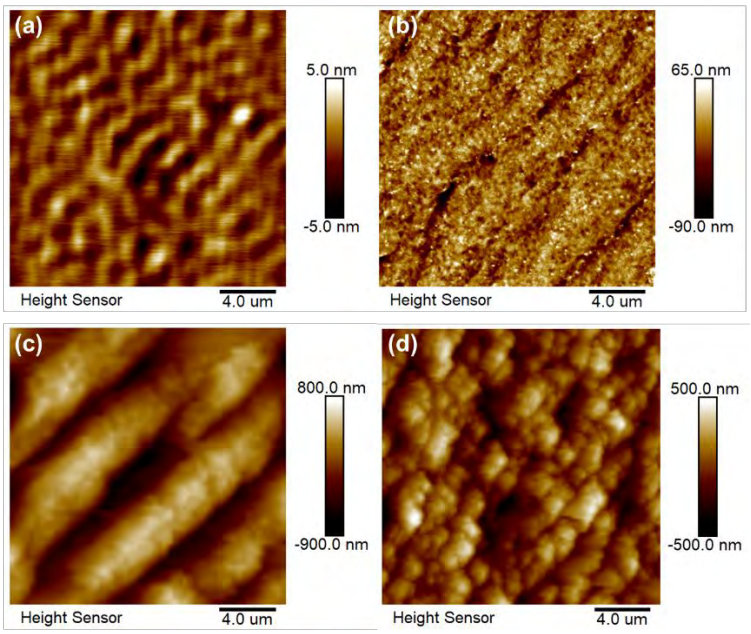

Figure S4. AFM images of MoS_2@PVA-LCO thin films with different LCO doping concentrations: (a) 0 wt%, (b) 10 wt%, (c) 35 wt% and (d) 50 wt%.

5. Electrical measurement of Pt/MoS_2@LCO-PVA/Si memristors.

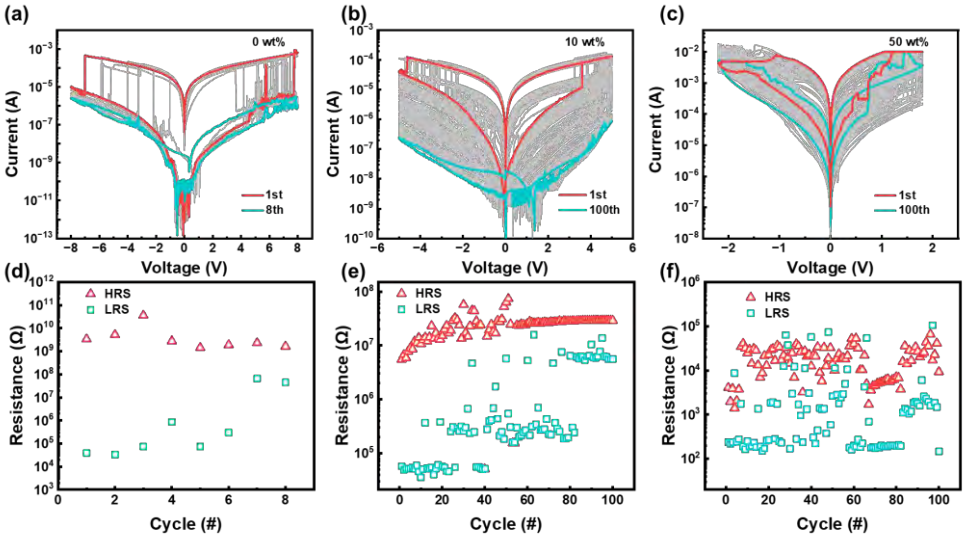

Figure S5. Electrical evaluation of Pt/MoS_2@LCO-PVA/Si memristors: *I-V* curves of (a) MoS_2@LCO_0-PVA based memristor, (b) MoS_2@LCO_{10}-PVA based memristor, and (c) MoS_2@LCO_{50}-PVA based memristor. Cycling stability of (d) MoS_2@LCO_0-PVA based memristor, (e) MoS_2@LCO_{10}-PVA based memristor, and (f) MoS_2@LCO_{50}-PVA based memristor.

Table S1. Properties of devices with different doping concentrations (10 wt%, 35 wt% and 50 wt%) for different cycles.

Devices	#Cycles	HRS C_v	LRS C_v
Pt/MoS_2@PVA-LCO/Si (0 wt%)	7 cycles	/	/
Pt/MoS_2@PVA-LCO/Si (10 wt%)	84 cycles	0.49	1.67
Pt/MoS_2@PVA-LCO/Si (35 wt%)	1670 cycles	0.26	0.63
Pt/MoS_2@PVA-LCO/Si (50 wt %)	100 cycles	0.67	2.96

6. The *I-V* characteristics of the uniformity of the devices

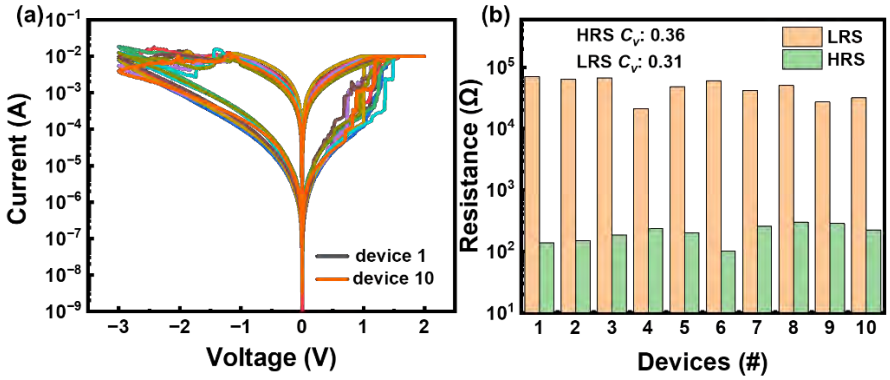

Figure S6. (a) The device-to-device variation is analyzed by scanning the voltage from 2 V to –3 V using a voltage step of ±0.01 V and I_{cc} of 0.01 A. (b) The statistical graph of HRS/LRS.

7. Compare the performance with various synaptic memristor reported.

Table S2. Summary of memristive properties (endurance, retention time, on/off ratios, and SET voltages) of different microstructural synaptic memristors such as quantum dots, nanosheets, nanoclusters, nanowires, and microrods (× denoting the parameter not mentioned in the references).

Structures	Endurance	Retention Time	On/Off Ratios	SET Voltages	Refs.
Au/PMMA/a-In_2Se_3/PMMA/ITO	500 cycles	1×10^4 s	~10^3	~ –1 V	1
Ag/Zn-TCPP@PMMA/Pt	100 cycles	×	~10^3	0.08 V	2
Ag/PVA:h-BN/ZrO_2/ITO	20 cycles	6×10^3 s	~10^3	~1 V	3

Ag-Cu/a-Si/Si	100 cycles	3.6×10^3 s	~10^2	~1.82 V	4
Ag/ZnO NS@TCPP/Pt	50 cycles	1×10^4 s	~4	–0.39 V	5
Au/MCA-BP/Au	10 cycles	4×10^3 s	10^4	4 V	6
Ag/Ni_3C-PVA/ITO/PET	100 cycles	1×10^4 s	2.09×10^2	2.8 V	7
Ag/$Zr_{0.5}Hf_{0.5}O_2$: GO QDs/Ag	100 cycles	1×10^4 s	×	~ 0.3 V	8
Pt/$LiCoO_2$/Si-QDs@SiO_x/Si	100 cycles	1×10^5 s	10^4	~ 4 V	9
Al/GO/SF/GO/ITO	100 cycles	>1×10^3	10^4	~ –2 V	10
Au/TiO_2 NW/Au	70 cycles	×	<10	6 V	11
Cu/HfO_2/TiO_2 NWA/FTO	100 cycles	>1×10^4 s	>10^2	~1 V	12
Ag/phenylalanine dipeptide (FF) microrod/Ag	2,000 cycles	×	10^4	~1.5 V	13
Al/ZnO NPs/CuO NWs/Cu	100 cycles	>8×10^3 s	~10^2	–1.5 V	14
AgNW-AgNP/SAM	100 cycles	1×10^5 s	>10^4	1.2 V	15
Al/PM6:MoS_2 QD/ITO	175 cycles	2×10^3 s	>10	0.3 ~ 0.6 V	16
Ag/PVP-MoS_2 QD/ITO	30 cycles	1.5×10^4 s	10^2	~1.3 V	17
Ag/peptide microrod/Ag	100 cycles	×	10^5	1.64 V	18
Pt/MoS_2@LCO-PVA/Si	**1,670 cycles**	**>3×10^4 s**	**~10^3**	**0.97 V**	**Our work**

8. Electric field distribution without dendritic structure.

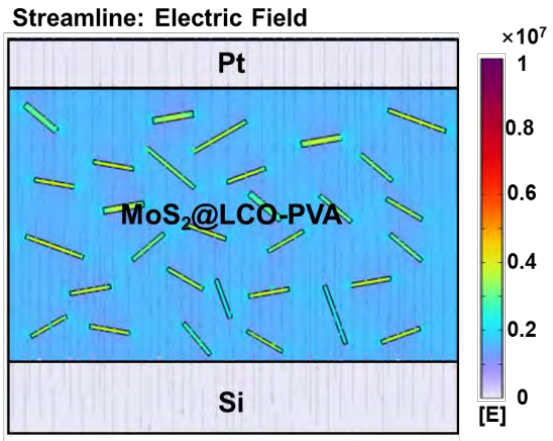

Figure S7. Electric field simulation of the device without dendritic structure using COMSOL Multiphysics software.

9. Schematic diagrams of the memristive mechanism model.

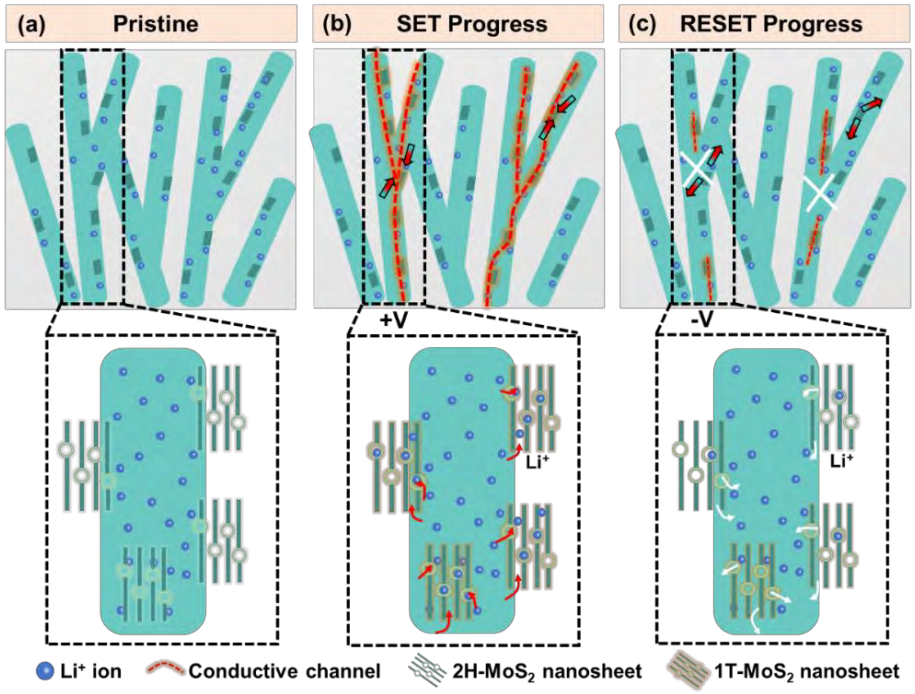

Figure S8. Schematic diagrams of the memristive mechanism model during (a) Pristine, (b) SET, and (c) RESET process.

10. The areal energy consumption of the Pt/MoS_2@LCO_{35}-PVA/Si based synaptic memristor.

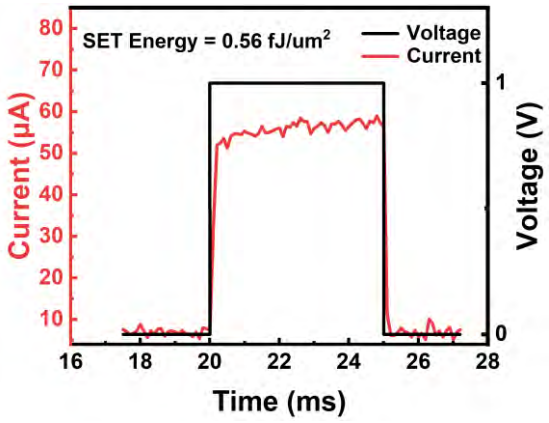

Figure S9. The areal energy consumption in the dendritic MoS_2@LCO-PVA based synaptic memristor with an electrical pulse (pulse amplitude = 1 V, pulse width = 5 ms).

Table S3. Comparison of the energy consumption for different microstructural and Li^+ based synaptic devices.

Structures (Functional layer)	Pulse amplitude	Pulse width	Energy Consumption	Refs.
PVA:h-BN/ZrO_2	3.0 V	0.5 s	9.1 nJ/um^2	3
$LiCoO_2$/Si-QDs@SiO_x	0.74 V	/	5.6 fJ/um^2	9
ZnO NPs/CuO NWs	1.0 V	5 s	20.6 fJ/um^2	14
WO_3/LiPON	10 μA	10 ns	100.0 fJ/um^2	19
NDI-gTVT/$LiClO_4$/PEO	1.0 V	0.04 s	7.4 pJ/um^2	20
WSe_2/$LiClO_4$/PEO	5.0 V	50 ms	10.0 fJ/um^2	21
Graphene/$LiClO_4$/PEO	50 pA	10 ms	13.9 fJ/um^2	22

$LiCoO_2/SiO_2$	50 nA	60 ms	1.46 fJ/um^2	23
α-Nb_2O_5/Li_xSiO_2	3.6 V	10 ms	20.0 fJ/um^2	24
$In_2O_3/Li_xAl_2O_3$	2.5 V	50 ms	63.0 fJ/um^2	25
MoS_2@LCO-PVA	**1.0 V**	**5ms**	**0.6 fJ/um^2**	**Our work**

References

(1) Ma, T.; Han, S.; Yang, D.; Ye, Y.; Liu, Y.; Shen, Z.; Li, F.; Li, H.; Chen, C. Two-Dimensional α-In_2Se_3 Memory Devices from Resistive Switching to Synaptic Plasticity. *Applied Physics Letters* **2023**, *123*, 263503.

(2) Wang, Y.; Su, J.; Ouyang, G.; Geng, S.; Ren, M.; Pan, W.; Bian, J.; Cao, M. Flexible Zn-TCPP Nanosheet-Based Memristor for Ultralow-Power Biomimetic Sensing System and High-Precision Gesture Recognition. *Advanced Functional Materials* **2024**, *34*, 2316397.

(3) Sun, T.; Yu, F.; Tang, X.; Li, H.; Zhang, F.; Xu, Z.; Liao, Q.; Yu, Z.; Liu, X.; Wangyang, P.; Li, H.; Peng, Y. Organic-2D Composite Material-Based Rram with High Reliability for Mimicking Synaptic Behavior. *Journal of Materiomics* **2024**, *10*, 440-447.

(4) Yeon, H.; Lin, P.; Choi, C.; Tan, S. H.; Park, Y.; Lee, D.; Lee, J.; Xu, F.; Gao, B.; Wu, H.; Qian, H.; Nie, Y.; Kim, S.; Kim, J. Alloying Conducting Channels for Reliable Neuromorphic Computing. *Nature Nanotechnology* **2020**, *15*, 574-579.

(5) Wang, Y.; Cao, M.; Bian, J.; Li, Q.; Su, J. Flexible ZnO Nanosheet-Based Artificial

Synapses Prepared by Low-Temperature Process for High Recognition Accuracy Neuromorphic Computing. *Advanced Functional Materials* **2022**, *32*, 2209907.

(6) Hsieh, Y. L.; Su, C. Y. Black Phosphorus Nanosheet/Melamine Cyanurate Assemblies as Functional Active Layers for Artificial Synapse Memristors. *ACS Applied Nano Materials* **2021**, *4*, 9584-9594.

(7) Koncha, G.; Das, N. K.; Badhulika, S. Ni_3C Nanosheets and PVA Nanocomposite Based Memristor for Low-Cost and Flexible Non-Volatile Memory Devices. *Materials Science in Semiconductor Processing* **2024**, *184*, 108804.

(8) Yan, X.; Zhang, L.; Chen, H.; Li, X.; Wang, J.; Liu, Q.; Lu, C.; Chen, J.; Wu, H.; Zhou, P. Graphene Oxide Quantum Dots Based Memristors with Progressive Conduction Tuning for Artificial Synaptic Learning. *Advanced Functional Materials* **2018**, *28*, 1803728.

(9) Gao, Q.; Huang, J.; Gao, J.; Geng, X.; Ji, Y.; Li, H.; Wang, G.; Liang, B.; Wang, M.; Xiao, Z.; Zhu, Y.; Chu, P. K.; Huang, A. Tunable Plasticity in Functionalized Honeycomb Synaptic Memristor for Neurocomputing. *Materials Today Physics* **2023**, *30*, 100947.

(10) Liu, S.; Cheng, Y.; Han, F.; Fan, S.; Zhang, Y. Multilevel Resistive Switching Memristor Based on Silk Fibroin/Graphene Oxide with Image Reconstruction Functionality. *Chemical Engineering Journal* **2023**, *471*, 144678.

(11) Zhao, B.; Xiao, M.; Zhou, Y. N. Synaptic Learning Behavior of a TiO_2 Nanowire Memristor. *Nanotechnology* **2019**, *30*, 425202.

(12) Sun, Y.; Wang, J.; He, D.; Yang, M.; Jiang, C.; Li, W.; Xiao, X. Enhanced Resistive

Switching Uniformity in HfO_2/TiO_2 NWA Memristor for Synaptic Simulation. *Applied Physics Letters* **2023**, *122*, 133501.

(13) Xing, X.; Huang, S.; Gong, Y.; Wang, J.; Lv, Z.; Zhou, Y.; Zhao, X.; Hao, J.; Han, S. T. Stochastic Current Response in Diffusive Memristor for Security Applications. *Materials Today Nano* **2023**, *22*, 100315.

(14) Wang, Y.; Wang, W.; Zhang, C.; Kan, H.; Yue, W.; Pang, J.; Gao, S.; Li, Y. A Digital-Analog Integrated Memristor Based on a ZnO NPs/CuO NWs Heterostructure for Neuromorphic Computing. *ACS Applied Electronic Materials* **2022**, *4*, 3525-3534.

(15) Chen, W.; Mou, Z.; Xin, Y.; Li, H.; Wang, T.; Chen, Y.; Chen, L.; Yang, B. R.; Chen, Z.; Luo, Y.; Liu, G. S. Self-Assembled Monolayer and Nanoparticles Coenhanced Fragmented Silver Nanowire Network Memristor. *ACS Applied Materials & Interfaces* **2024**, *16*, 6057-6067.

(16) Zhang, Q.; Jiang, Q.; Fan, F.; Liu, G.; Chen, Y.; Zhang, B. MoS_2 Quantum Dot-Optimized Conductive Channels for a Conjugated Polymer-Based Synaptic Memristor. *ACS Applied Materials & Interfaces* **2023**, *15*, 59630-59642.

(17) Li, M.; An, H.; Kim, Y.; An, J. S.; Li, M.; Kim, T. W. Directional Formation of Conductive Filaments for a Reliable Organic-Based Artificial Synapse by Doping Molybdenum Disulfide Quantum Dots into a Polymer Matrix. *ACS Applied Materials & Interfaces* **2022**, *14*, 44724-44734.

(18) Lv, Z.; Xing, X.; Huang, S.; Wang, Y.; Chen, Z.; Gong, Y.; Zhou, Y.; Han, S. T. Self-Assembling Crystalline Peptide Microrod for Neuromorphic Function

Implementation. *Matter* **2021**, *4*, 1702-1719.

(19) Tang J.; D. B.; Kim S.; Copel M.; Gokmen T.; Todorov T.; Shin S.; Lee K.; Solomon P.; Chan K.; Haensch W.; Rozen J. Ecram as Scalable Synaptic Cell for High-Speed, Low-Power Neuromorphic Computing. *IEEE International Electron Devices Meeting* **2018**, 13.11.11-13.11.14.

(20) Xie, Z.; Zhuge, C.; Zhao, Y.; Xiao, W.; Fu, Y.; Yang, D.; Zhang, S.; Li, Y.; Wang, Q.; Wang, Y.; Yue, W.; McCulloch, I.; He, D. All-Solid-State Vertical Three-Terminal N-Type Organic Synaptic Devices for Neuromorphic Computing. *Advanced Functional Materials* **2022**, *32*, 2107314.

(21) Zhu, J.; Yang, Y.; Jia, R.; Liang, Z.; Zhu, W.; Rehman, Z. U.; Bao, L.; Zhang, X.; Cai, Y.; Song, L.; Huang, R. Ion Gated Synaptic Transistors Based on 2D Van Der Waals Crystals with Tunable Diffusive Dynamics. *Advanced Materials* **2018**, *30*. 1800195.

(22) Sharbati, M. T.; Du, Y.; Torres, J.; Ardolino, N. D.; Yun, M.; Xiong, F. Low-Power, Electrochemically Tunable Graphene Synapses for Neuromorphic Computing. *Advanced Materials* **2018**, *30*, 1802353.

(23) Chen, Y.; Zhang, W.; Lu, Y.; Chen, M.; Chen, J.; Lu, H.; Niu, Y.; Zhao, G.; Tao, J.; Li, J.; Lin, Y.; Kolosov, O.; Huang, Z. Inhibiting the Current Spikes within the Channel Layer of $LiCoO_2$-Based Three-Terminal Synaptic Transistors. *Applied Physics Reviews* **2024**, *11* ,041407.

(24) Li, Y.; Lu, J.; Shang, D.; Liu, Q.; Wu, S.; Wu, Z.; Zhang, X.; Yang, J.; Wang, Z.; Lv, H.; Liu, M. Oxide-Based Electrolyte-Gated Transistors for Spatiotemporal

Information Processing. *Advanced Materials* **2020**, *32*, 2003018.

(25) Jiang, D.; Li, J.; Fu, W.; Chen, Q.; Yang, Y.; Zhou, Y.; Zhang, J. Light-Stimulated Artificial Synapse with Memory and Learning Functions by Utilizing an Aqueous Solution-Processed In_2O_3/AlLiO Thin-Film Transistor. *ACS Applied Electronic Materials* **2020**, *2*, 2772-2779.